

Technical note: High-resolution analyses of concentrations and sizes of refractory black carbon particles deposited on northwest Greenland over the past 350 years – Part 1. Continuous flow analysis of the SIGMA-D ice core using a Wide-Range Single-Particle Soot Photometer and a high-efficiency nebulizer

Kumiko Goto-Azuma^{1,2}, Remi Dallmayr^{1,a}, Yoshimi Ogawa-Tsukagawa¹, Nobuhiro Moteki³, Tatsuhiro Mori⁴, Sho Ohata⁵, Yutaka Kondo¹, Makoto Koike⁶, Motohiro Hirabayashi¹, Jun Ogata¹, Kyotaro Kitamura¹, Kenji Kawamura^{1,2}, Koji Fujita⁵, Sumito Matoba⁷, Naoko Nagatsuka^{1,c}, Akane Tsushima^{1,b}, Kaori Fukuda¹, and Teruo Aoki¹

¹National Institute of Polar Research, Tachikawa, Tokyo, 190-8518, Japan

²SOKENDAI, Shonan Village, Hayama, Kanagawa, 240-0193, Japan

³Tokyo Metropolitan University, Hachioji, Tokyo, 192-0397, Japan

⁴Keio University, Yokohama, Kanagawa, 223-8521, Japan

⁵Nagoya University, Nagoya, 464-8601, Japan

⁶University of Tokyo, Bunkyo-ku, 113-0033, Japan

⁷Hokkaido University, Sapporo, 060-0819, Japan

^aNow at Alfred Wegener Institute for Polar and Marine Research, Bremerhaven, Germany

^bNow at Meteorological Research Institute, Tsukuba, Ibaraki, 305-0052, Japan

^cNow at Japan Agency for Marine-Earth Science and Technology, Yokosuka, Kanagawa, 237-0061, Japan

Correspondence to: Kumiko Goto-Azuma (kumiko@nipr.ac.jp)

Abstract. Ice cores can provide long-term records of refractory black carbon (rBC), an important aerosol species closely linked to the climate and environment. However, previous studies of ice cores only analysed rBC particles with diameter of <500nm, which could have led to underestimation of rBC mass concentrations. Information on the size distribution of rBC particles is very limited, and there are no Arctic ice core records of the temporal variation in rBC size distribution. In this study, we applied a recently developed improved technique to analyse the rBC concentration in an ice core drilled at the SIGMA-D site in northwest Greenland. The improved technique, which uses a modified Single-Particle Soot Photometer and a high-efficiency nebulizer, widens the measurable range of rBC particle size. For high-resolution continuous analyses of ice cores, we developed a continuous flow analysis (CFA) system. Coupling of the improved rBC measurement technique with the CFA system allows accurate high-resolution measurements of the size distribution and concentration of rBC particles with diameter between 70 nm and 4 μm , with minimal particle losses. Using this technique, we reconstructed the size distributions and the

32 number and mass concentrations of rBC particles during the past 350 years. On the basis of the size distributions, we assessed
33 the underestimation of rBC mass concentrations measured using the conventional SP2s. For the period 2003–2013, the
34 underestimation of the average mass concentration would have been 12%–31% for the SIGMA-D core.

35 **1 Introduction**

36 Black carbon (BC), which is emitted from both anthropogenic and natural sources (e.g., fossil fuel combustion and biomass
37 burning), can affect Earth’s radiation budget by absorbing sunlight and reducing the albedo of snow and ice surfaces (e.g.,
38 Bond et al., 2013; Mori et al., 2019; Matsui et al., 2022; Moteki, 2023 and references therein). Particles of BC can also affect
39 cloud microphysical processes by acting as cloud condensation nuclei (CCN) or ice nucleating particles (e.g., Bond et al.,
40 2013; AMAP, 2021), thereby indirectly affecting the radiation budget. Over the past half-century, the Arctic has warmed at a
41 rate four times faster than that of the global average (Rantanen et al., 2022), leading to drastic changes such as sea ice retreat,
42 enhanced losses of glacier mass, and ecosystem changes. It is therefore important to evaluate the effects of BC on the radiation
43 budget in the Arctic. Freshly emitted BC particles are initially hydrophobic, but gradually become coated with other aerosol
44 species, transforming into internally mixed hydrophilic particles during transport (*e.g.* Mori et al., 2017; Matsui, 2017; Matsui
45 and Mahowald, 2017). These hydrophilic BC particles can be activated as CCN, depending on their size and mixing state, and
46 are eventually deposited on the earth’s surface via precipitation. The size distribution of BC particles influences not only their
47 ability to act as CCN but also their transport and deposition processes, thereby controlling the temporal and spatial variability
48 of BC concentrations. In addition, size distribution affects the light absorption properties of BC particles. Therefore, the size
49 distribution as well as concentrations of BC particles is a key parameter for understanding the impacts of BC on Earth’s
50 radiation budget. Data acquired since the pre-industrial period are particularly valuable because we cannot fully understand
51 the anthropogenic effects without characterizing BC in a pristine environment. However, no direct measurements of the size
52 distributions and concentrations of BC particles were performed prior to the past few decades despite numerous studies based
53 on observations and aerosol/climate models (e.g., Bond et al., 2013 and references therein).

54 Ice cores can provide long-term records of BC deposition. Following development of the Single-Particle Soot
55 Photometer (SP2; Droplet Measurement Technologies, USA) (Stephens et al., 2003; Baumgardner et al., 2004), it has been
56 possible to measure refractory black carbon (rBC), the terminology used for incandescence-based BC measurements (Petzold et
57 al., 2013; Lim et al., 2014), even in Arctic and Antarctic ice cores that contain very low concentrations of rBC particles

58 (McConnell et al., 2007; Zdanowicz et al., 2018; Osmont et al., 2018; Zennaro et al., 2014; Bisiaux et al., 2012a, b; Arienzo
59 et al., 2019). Moreover, attachment of a coupled SP2 and nebuliser system to a continuous flow analysis (CFA) system allowed
60 continuous and high temporal-resolution analyses of rBC in ice cores drilled at a site with little summer melting (McConnell
61 et al., 2007; Lim et al., 2017; Bisiaux et al., 2012a, 2012b; Arienzo et al., 2017). Many previous SP2 analyses of rBC in ice
62 cores, regardless of whether they used a CFA system, adopted the U5000AT ultrasonic nebuliser (Teledyne CETAC, USA)
63 system (or a similar ultrasonic nebuliser) to aerosolize rBC particles in melted ice core samples before their introduction to the
64 SP2 (McConnell et al., 2007; Zennaro et al., 2014; Zdanowicz et al., 2018; Du et al., 2020; Kaspari et al., 2011; Wang et al.,
65 2015; Bisiaux et al., 2012a, 2012b; Arienzo et al., 2017). Owing to the complex and temporally variable size dependence of the
66 extraction efficiency of the U5000AT ultrasonic nebuliser system (Schwarz et al., 2012; Wendl et al., 2014; Ohata et al., 2013;
67 Mori et al., 2016), large uncertainties are associated with the derived size distributions and concentrations. Obtaining accurate
68 estimation of the size distribution of rBC particles on a routine basis is not easy using the U5000AT nebulizer system. While
69 Kaspari et al. (2011) reported mass size distributions of rBC in two samples from a Mt. Everest ice core using the U5000AT
70 nebulizer system, long-term ice core records of the size distribution of rBC particles obtained using this type of nebulizer
71 system have not been reported. On the contrary, Wendl et al. (2014) demonstrated size-independent extraction efficiency
72 (<15% variability) of the APEX Q jet nebulizer system (High-Sensitivity Sample Introduction System, Elemental Scientific
73 Inc., USA) for rBC particles in the 100-1000 nm diameter range. Lim et al. (2014) also reported size-independent extraction
74 efficiency (<10% variability) of the APEX Q nebulizer system for rBC particles with diameters between 60 and 500 nm. As a
75 result, recently, the APEX-Q nebulizer system is becoming the standard within the ice core community. Using an APEX Q
76 nebulizer system and an SP2 attached to a CFA system, Lim et al. (2017) analysed ice cores from Mt. Elbrus (western Caucasus
77 Mountains) and reported temporal variability in the size and concentration of rBC particles with diameters between 70 and
78 620 nm during 1825–2013. However, to date, no rBC size distribution data from Arctic ice cores have been published.

79 Snow and hence ice cores could contain much larger rBC particles than those typically observed in the atmosphere
80 (Schwarz et al., 2012, 2015). The particle size range typically measurable by an off-the-shelf SP2 is from approximately 70 to
81 400-500 nm (Moteki and Kondo, 2010; Kaspari et al., 2011), i.e., particles with diameter of >500 nm cannot be detected using
82 an off-the-shelf SP2. Moteki and Kondo (2010) extended the upper limit of measurable rBC particle diameters to 850-900 nm
83 (Moteki and Kondo, 2010; Ohata et al., 2011). More recently, an off-the-shelf instrument called the Single Particle Soot

84 Photometer Extended Range (SP2-XR; Droplet Measurement Technologies, USA), with measurable diameter range 50-800
85 nm, has become available. However, to our knowledge, no ice core rBC data produced by the SP2-XR have been published.

86 The extraction efficiency of the U5000AT ultrasonic nebulizer system at a flow rate of 0.19 mL min^{-1} has been
87 reported to be 10%–12% for the particle diameter range of approximately 200–500 nm; it decreases sharply for diameters >500
88 nm and decreases to approximately 2% for particles with diameter of 700 nm (Ohata et al., 2013; Mori et al., 2016). It also
89 decreases for diameters < 200 nm (Ohata et al., 2013; Wendl et al., 2014; Mori et al., 2016). Thus, unless the size dependent
90 extraction efficiency is carefully measured, as done by Moteki and Kondo (2010) and Ohata et al. (2011), measurements
91 obtained using this nebulizer system could have large uncertainties not only in size distribution but also in mass concentration
92 if the ice core samples contain BC particles with diameter of >500 nm, even if an SP2 with extended upper limit is used.

93 Modern snow and ice core samples from the Arctic, including Greenland, do contain substantial fractions of rBC
94 particles with diameter of >500 nm (Mori et al., 2019). Similarly, modern snow from Antarctica also contains a considerable
95 proportion of rBC particles with diameters >500 nm (Kinase et al., 2020). If mass size distributions follow lognormal size
96 distributions with mass median diameters <500 nm, mass concentrations for diameters > 500 nm can be estimated using
97 lognormal fitting. However, non-lognormal mass size distributions with substantial concentrations of particles with diameters
98 >850-900 nm have been reported for Arctic snow (Mori et al., 2019). Non-lognormal mass size distributions have also been
99 observed in a Mt. Everest ice core, which contained substantial mass concentrations of rBC particles larger than the upper
100 measurable diameter limit of 500 nm (Kaspari et al., 2011). Furthermore, bimodal mass size distributions with secondary
101 modes diameters >500 nm have been reported for Antarctic snow (Kinase et al., 2020). Therefore, it is important to extend the
102 measurable diameter range of rBC particles beyond 900 nm and to employ a nebulizer system with a high and size-independent
103 extraction efficiency.

104 Mori et al. (2016) developed an improved technique for accurate measurement of the size distributions and
105 concentrations of rBC particles with diameter between 70 nm and $4 \mu\text{m}$ in water samples. They used a Wide-Range SP2 (i.e.,
106 an SP2 modified to widen the measurable size range of rBC particles) and a Marin-5 high-efficiency concentric pneumatic
107 nebulizer system (Teledyne CETAC, USA). For accurate, continuous, and high-resolution analyses of the concentrations and
108 size distributions of rBC particles in polar ice cores, we combined the improved rBC measurement technique and a CFA system
109 developed at the National Institute of Polar Research (NIPR). We used this system to analyse an ice core drilled at SIGMA-D
110 in northwest Greenland (Matoba et al., 2015; Nagatsuka et al., 2021), following which we reconstructed the concentrations

111 and size distributions of rBC particles with diameter between 70 nm and 4 μm for the past 350 years. In this paper (called Part
112 1), we describe the coupled CFA-rBC measurement system and evaluate its performance. We compare the nebulizer
113 efficiencies of Marin-5, APEX-Q, and U5000AT nebulizer systems; assess the stability of the efficiency of Marin-5 nebulizer
114 system; examine the dispersion of the CFA-rBC signal; provide the evidence of minimal losses of rBC particles within the
115 CFA-rBC system; and show examples of rBC size distributions. Since it is important to compare the data that our new rBC
116 measurement system produced and the valuable data from the previous ice core rBC measurements, we also estimated the
117 extent of underestimations in mass concentrations measured with the off-the-shelf SP2s. Using the new continuous high-
118 resolution data, we investigated the seasonal variations in concentrations and size distributions of rBC particles originating
119 from both anthropogenic and biomass burning emissions and their temporal changes. In a companion paper (Part 2), we discuss
120 the derived results in detail.

121 **2 Methods**

122 **2.1 Continuous flow analysis (CFA) system**

123 To undertake high-resolution continuous analyses of ice cores, we developed a CFA system at NIPR. Figure 1 shows a
124 schematic of the NIPR CFA system used to analyse the SIGMA-D core. It consists of a melting unit, debubbler unit, inductively
125 coupled plasma–mass spectrometer (ICP-MS) unit, stable water isotope unit, microparticle unit, methane unit, and fraction
126 collector unit in addition to an rBC unit. The rBC unit, ICP-MS unit, microparticle unit, and methane unit were added to an
127 earlier version of the NIPR CFA system described by Dallmayr et al. (2016). The melting unit, debubbler unit, and the stable
128 water isotope unit were the same as those used in the earlier version. Details of the melting unit, the ICP-MS unit, and the
129 stable water isotope unit are provided in Appendix A. Although the NIPR CFA system includes a microparticle unit, methane
130 unit, and fraction collector unit consisting of three fraction collectors, we do not discuss them further here because the data
131 that they provided are not relevant. The specification and performance of each of these units will be reported elsewhere.

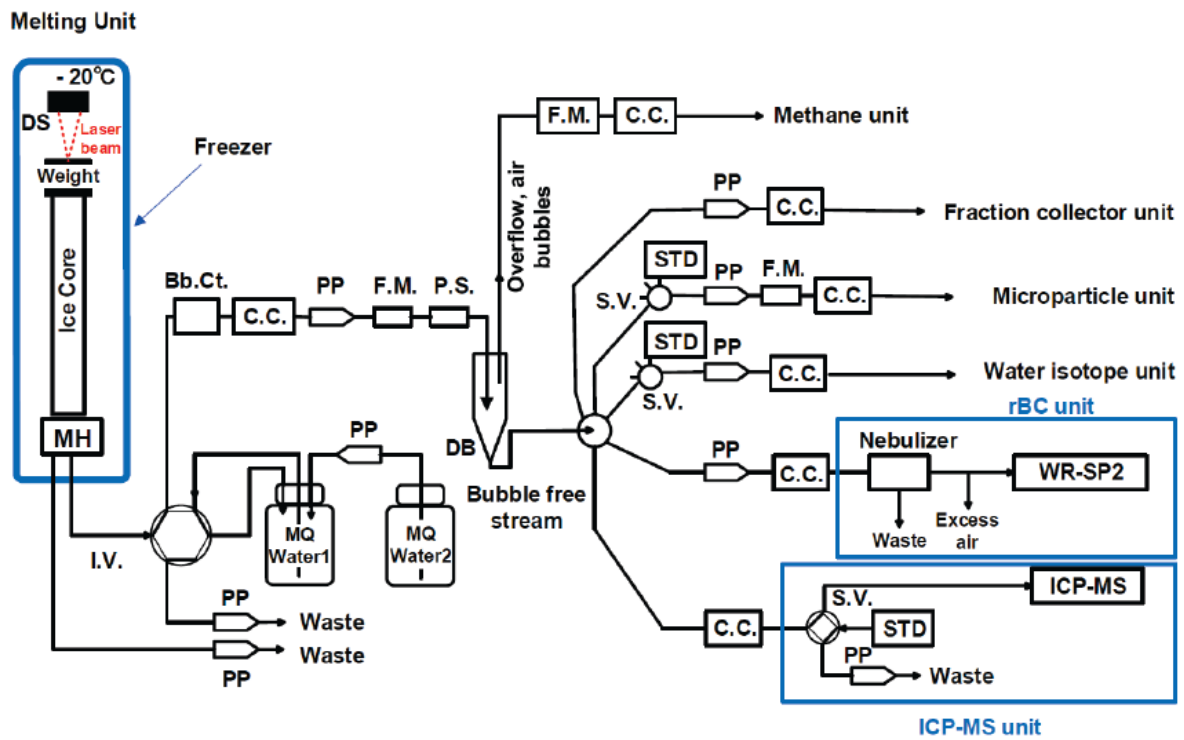


Figure 1: Schematic of the CFA system developed in this study.

DS: displacement sensor, MH: melt head, I.V.: injection valve, S.V.: selection valve, Bb.Ct.: bubble counter, C.C.: conductivity cell, PP: peristaltic pump, F.M.: flow meter, P.S. pressure sensor, DB: debubbler, STD: standard, MQ Water: ultra-pure water generated by a Milli-Q system.

133 2.2 Refractory black carbon (rBC) unit

134 We applied the improved technique developed by Mori et al. (2016) to the rBC unit of the NIPR CFA system. The rBC unit
 135 consists of a Wide-Range SP2 (Mori et al., 2016) and a concentric pneumatic nebulizer system (Marin-5, Teledyne CETAC,
 136 USA). The SP2 detects the incandescence signal from individual rBC particles induced by irradiation of an Nd-YAG laser
 137 (Stephens et al., 2003; Baumgardner, 2004; Schwarz et al., 2006). The off-the-shelf SP2 can detect rBC particles with diameter
 138 of between 70 and 400–500 nm, assuming rBC particle density of 1.8 g cm^{-3} (Moteki and Kondo, 2010; Kaspari et al., 2011).
 139 The SP2 modified by Moteki and Kondo (2010) can measure rBC particles with diameters between approximately 70 and
 140 850-900 nm, whereas the off-the-shelf SP2-XR can measure rBC particles with diameters between approximately 50 and 800
 141 nm. For the Wide-Range SP2, Mori et al. (2016) expanded the upper limit of the measurable diameter to $4 \mu\text{m}$ by modifying

142 the detection unit of the standard SP2. As a result, the Wide-Range SP2 can detect rBC particles with diameters of between
143 approximately 70 nm and 4 μm . We used the “Standard SP2 Software” and the “Probe Analysis Package for Igor (PAPI)”,
144 both provided by DMT, to acquire and process the incandescent signal in binary data and convert it to text format. Then
145 we used our original code to calculate the mass and size of BC particles.

146 The meltwater that passes through the debubbler unit is fed to the Marin-5 nebulizer system at a constant flow rate of
147 $6.3 \mu\text{L s}^{-1}$ by a peristaltic pump (REGLO Digital ISM596, ISMATEC, Germany) running at 7.50 rpm. We measured the flow
148 rate before and after each CFA session. As the flow rate slightly (~5%) decreased after each CFA session, likely due to tube
149 wear, we adjusted the flow rate of the peristaltic pump before the next CFA session. This approach allowed us to maintain a
150 nearly constant flow rate with less than 5% variability. Under these conditions, no pulsed flow was observed. The Marin-5
151 nebulizer system was equipped with a MicroMist U-Series nebulizer AR30-1-UM05E (Glass Expansion, Australia). We used
152 G3 Grade air as a carrier gas for the nebulizer. The flow rate of the carrier gas was $15.2 \text{ cm}^3 \text{ s}^{-1}$ at standard temperature and
153 pressure (i.e., 0 $^{\circ}\text{C}$ and 1013 hPa, respectively). The nebulizer system converts a fraction of the meltwater into water droplets
154 that are immediately heated to 140 $^{\circ}\text{C}$ in a spray chamber, generating a mixture of rBC particles, non-rBC particles, and water
155 vapor. After the non-aerosolized meltwater is removed via the drains, this mixture is cooled to 3 $^{\circ}\text{C}$ in a condenser, thereby
156 removing the water vapor. Hence, only rBC and non-rBC particles are introduced to the Wide-Range SP2 at a flow rate of 12
157 $\text{cm}^3 \text{ min}^{-1}$. The details of the Wide-Range SP2 and the Marin-5, together with assessment of their performance, have been
158 reported by Mori et al. (2016).

159 To derive the relationship between the peak incandescence signal and the mass of each rBC particle (Stephens et al.,
160 2003; Schwarz et al., 2006), we used fullerene soot (Alpha Aesar Inc., USA, Lot No. 20W054) as a standard material (Moteki
161 and Kondo, 2010). We used an Aerosol Particle Mass Analyzer (Moteki and Kondo, 2010) Model 3601 (APM-II, KANOMAX,
162 Japan) to extract fullerene soot particles with a mass range of 1.19–203 fg, corresponding to mass equivalent diameters of
163 100–600 nm. Following Mori et al. (2016), we produced two calibration curves for rBC masses below and above 10 fg, which
164 corresponds to the mass equivalent diameter of 220 nm. Mass equivalent diameters of rBC particles were calculated assuming
165 an rBC particle density of 1.8 g cm^{-3} (Moteki and Kondo, 2010).

166 For accurate measurement of rBC particle size, the nebulizer efficiency and its size dependence must be known (Ohata
167 et al., 2013; Mori et al., 2016). However, to the best of our knowledge, previous ice core studies using an SP2 rarely used
168 nebulizer efficiency determined by measurements, except those conducted by Wendl et al. (2014), Lim et al. (2014) and Lim

169 et al. (2017). We determined nebulizer efficiency using Polystyrene Latex Sphere (PSL) suspensions with known number
170 concentrations (Ohata et al., 2011, 2013; Mori et al., 2016) for diameters of >200 nm. We used PSL particles supplied by two
171 manufacturers. The diameters of the PSL particles supplied by Polysciences Inc., USA (NIST Traceable Particle Size Standard),
172 were 207, 288, 505, 603, 707, 814, 1025, and 1537 nm, and the diameters of those supplied by Thermo Fisher Scientific Inc.,
173 USA, were 2000 and 3000 nm. For diameters of <200 nm, we used AquaBlack 162 (AB-162, Tokai Carbon Co. Ltd., Japan),
174 which is a laboratory standard for rBC particles suspended in water (Mori et al., 2016; Ohata et al., 2011; Ohata et al., 2013).
175 The number concentration of the PSL particles and that of the AquaBlack samples in the carrier gas were measured by the
176 Wide-Range SP2, and compared with those of the PSL suspensions and the B-162 suspensions, respectively, to calculate
177 nebulizer efficiency. Measurements of the PSL suspensions were performed with the SP2 laser currents lower than those for
178 rBC measurements. We repeatedly measured the efficiency of the Marin-5 nebulizer system over a ten year period.
179 Additionally, we measured the efficiency of the APEX-Q and U5000AT nebulizer systems. For the APEX-Q nebulizer system,
180 we used two types of nebulizers: the Conikal Nebulizer AR30-1-FC1ES (Glass Expansion, Australia) and the MicroMist U-
181 Series nebulizer AR30-1-UM05E (Glass Expansion, Australia), the latter being the same one used in the Marin-5 nebulizer
182 system.

183 Number and mass concentrations of rBC particles in the melted ice core samples were calculated using the nebulizer
184 efficiency (Mori et al., 2016). The combination of the Wide-Range SP2 and the Marin-5 nebulizer system provides a
185 measurable diameter range of 70 nm to 4 μm . With this rBC unit attached to the melting and debubbler units, we acquired
186 number concentrations, mass concentrations, and mass equivalent diameters of rBC particles every second. The detection
187 limits of rBC number and mass concentrations in water samples, determined as 3σ of the blank values, were approximately 10
188 $\text{counts}\cdot\text{L}^{-1}$ and $0.01\ \mu\text{g}\cdot\text{L}^{-1}$, respectively. The accuracy of the rBC number and mass concentrations in the water samples was
189 approximately 16%, which was derived from the measurement uncertainties of the peristaltic pump flow rate ($\pm 5\%$), nebulizer
190 flow rate ($\pm 5\%$), nebulizer efficiency ($\pm 10\%$), and rBC concentration in the carrier gas measured by the SP2 ($\pm 10\%$) (Mori et
191 al., 2016, 2021). The reproducibility of the number and mass concentrations for repeated measurements of the same melted
192 ice core and Arctic snow samples on two different days was usually better than 10% (Mori et al., 2019). For example, Mori et
193 al. (2019) demonstrated that the mass and number concentrations of rBC particles in a melted sample from the SIGMA-D core,
194 analysed on the day it was melted and again 21 months later, showed agreement within 5.6% and 4.4%, respectively. Mori et
195 al. (2019) further demonstrated that the changes in the mass and count median diameters were negligibly small in this sample.

196 Additionally, possible changes in the count median diameter during the nebulizing process were estimated to be only 2 nm for
197 the fullerene soot, whose count median diameter was ~120 nm and whose mass concentration in water was 6.9–64 $\mu\text{g}\cdot\text{L}^{-1}$
198 (Mori et al., 2016). A similar value was estimated for the AB-162. These experimental results suggest that the shape of the
199 rBC size distribution and the rBC mass concentration changed little during the nebulizer extraction process.

200 rBC particles could stick to the various components of the CFA system such as the melt head, debubbler, valves,
201 conductivity cells, tubing, and nebulizer system, which could reduce the concentration and change the size distribution. We
202 investigated whether losses of rBC particles occurred in the CFA system. We injected a melted surface snow sample from
203 SIGMA-A (northwest Greenland) (Matoba et al., 2018) from above the centre hole of the melt head, and measured the
204 concentration and size distribution of BC particles. We used the University of Copenhagen type melt head for this test. We
205 also injected the same sample directly into the Marin-5 nebulizer system and measured the concentration and size distribution
206 of rBC particles. We then compared the results of the two experiments to check whether any changes occurred that could be
207 attributed to the CFA system.

208

209 **2.3 Signal dispersion tests**

210 The mixing of meltwater, which occurs in parts of the CFA system such as the melt head, debubbler, valves, conductivity cells,
211 tubing, and nebulizer system, causes signal dispersion and reduces the resolution of the CFA data. To evaluate the signal
212 dispersion, we examined the response of each unit by switching between injection of ultra-pure water and injection of standard
213 solutions or melted ice core/snow samples at the melt heads (Bigler et al., 2011). The ultra-pure water, standard solutions, and
214 melted ice core/snow samples were injected from above the centre hole of the melt heads. The ultra-pure water used in this
215 study was made using a Milli-Q Advantage system (Merck Millipore, Germany). The samples used for the dispersion tests are
216 listed in Table 1.

217

218 **Table 1. List of samples for signal dispersion tests**

Measurement	Type of test samples
rBC	AquaBlack 162 (AB-162, Tokai Carbon Co. Ltd.)
ICP-MS	Surface snow from Dome Fuji, Antarctica, concentrated by heating

219 **2.4 Processing and analyses of the SIGMA-D ice core**

220 A 222.7 m ice core was drilled at the SIGMA-D site (77.636° N, 59.120° W; 2100 m a.s.l.) in northwest Greenland in spring
221 2014 (Matoba et al., 2015). The annual mean air temperature and accumulation rate at the site were estimated to be $-25.6\text{ }^{\circ}\text{C}$
222 and 0.23 w eq yr^{-1} (Nagatsuka et al., 2021), respectively. In the field, the top 175.77 m of the core was divided into two vertical
223 sections (Sections A and B).

224 Section A was kept frozen and transported to NIPR in Japan. We analysed the depth interval between 6.17 and 112.87
225 m of this section using the CFA system described in Sect. 2.1 and 2.2. The top 6.17 m of this section was too fragile to be
226 analysed with the CFA system; hence, we manually cut segments of approximately 0.1 m. These discrete samples were
227 decontaminated in a cold room ($-20\text{ }^{\circ}\text{C}$) using a precleaned ceramic knife, and then placed in powder-free plastic bags. They
228 were then melted and transferred to precleaned glass and polypropylene bottles in a class 10,000 clean room. The samples in
229 glass bottles were analysed for stable water isotopes and rBC, whereas those in polypropylene bottles were analysed for six
230 elements using an ICP-MS. Analyses of stable water isotopes and six elements are described in Appendix B1. The rBC was
231 analysed using a Wide-Range SP2 (Mori et al., 2016) and a concentric pneumatic nebulizer system (Marin-5, Teledyne CETAC,
232 USA), i.e., the same as those in the NIPR CFA system. The setting and analytical conditions of the Wide-Range SP2 and
233 Marin-5 were similar to those described in Sect. 2.2. Concentrations and diameters of rBC particles were calibrated in the same
234 way as described in Sect. 2.2.

235 Section B was cut in the field into 0.06–0.12 m long vertical segments for the top 5 m of the core, 0.05–0.08 m long
236 segments for depths of 5–12 m, and approximately 0.05 m long segments for the depth interval between 12 and 112.87 m.
237 Each segment was placed in a plastic bag, melted, and transferred to a precleaned polypropylene bottle in the field. The discrete
238 samples contained in the polypropylene bottles were refrozen in the field, transported to Japan, and kept frozen until analysis,
239 whereupon they were melted and analysed for major ions and stable water isotopes (Nagatsuka et al., 2021). Analyses of the
240 discrete samples from Section B are described in Appendix B2.

241 **3 Results and Discussion**

242 **3.1 Nebulizer efficiency**

243 Figure 2 shows the efficiency of the Marin-5 nebulizer system for different flow rates of meltwater. As previously reported
 244 (Mori et al., 2016), nebulizer efficiency depends on flow rate. For three flow rates—0.19, 0.38, and 0.48 mL·min⁻¹—the
 245 efficiency was almost constant for diameters of <2000 nm, and it declined linearly with diameter for diameters >2000 nm, as
 246 reported by Mori et al. (2016). For a flow rate of 0.38 mL·min⁻¹, which is the flow rate used in the NIPR CFA system, the
 247 efficiency was 34.2% ± 8.0% for particles with diameter of <2000 nm, and it declined linearly with diameter for diameters of
 248 2–4 μm. The efficiency of Marin-5 was slightly higher than that of APEX-Q for the PSL with diameters between 200 and 700
 249 nm at a flow rate of 0.38 mL min⁻¹ (Fig.C1(a)). Repeated measurements of the Marin-5 efficiency over a ten-year period (Fig.
 250 3) indicate that the nebulizer efficiencies remained stable over time, despite some fluctuation around the regression lines. For
 251 particles with diameters < 2 μm, the variability was ±8 %, which does not significantly affect the rBC data. Consequently, we
 252 applied the same nebulizer efficiency values across all CFA sessions. Additionally, we validated the stability of our WR-
 253 SP2/nebulizer system by repeatedly measuring the rBC mass and number concentrations in the same samples, as demonstrated
 254 by Mori et al. (2019). In contrast to the Marin-5 nebulizer system, the U5000AT nebulizer system exhibited size- and time-
 255 dependent efficiency (Fig. C2(b)).
 256

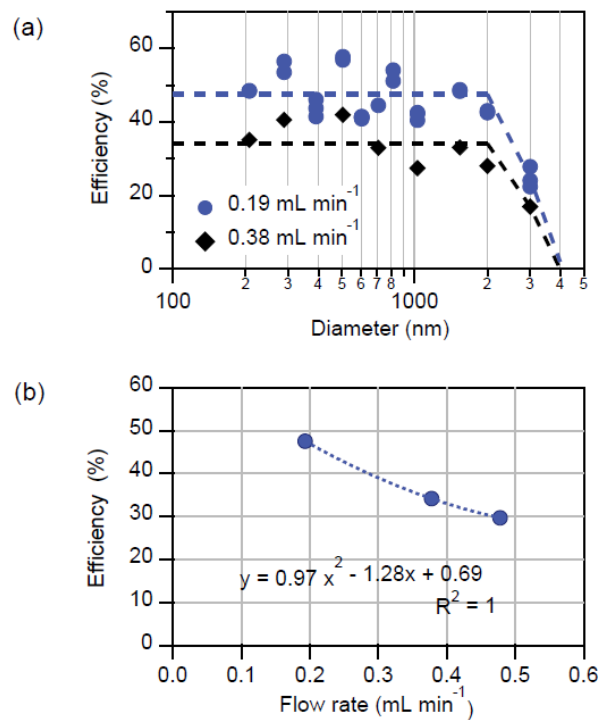


Figure 2: Dependence of Marin-5 nebulizer efficiency on (a) BC diameter for two flow rates and (b) flow rate for BC diameter of <2 μm.

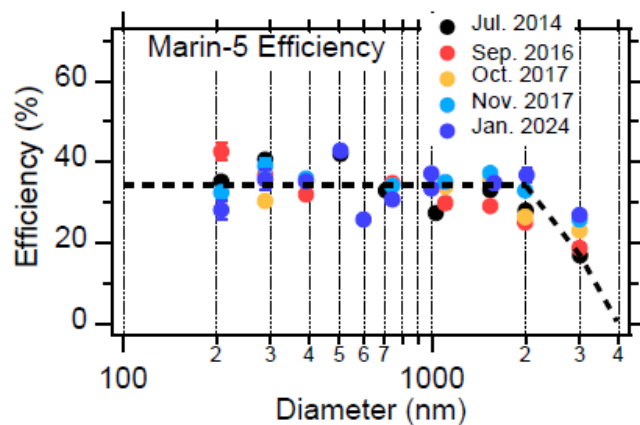


Figure 3: Repeated measurements of Marin-5 nebulizer efficiency over ten years for a flow rate 0.38 mL L^{-1} .

258

259 3.2 Signal dispersion

260 Figure 4 displays the results of dispersion tests for $\delta^{18}\text{O}$, Na, and rBC. We defined two types of response times: (1) the time

261 (t1) required for transition from 10% of the standard (or ice core/snow sample) value to 90% of the standard (or ice core/snow

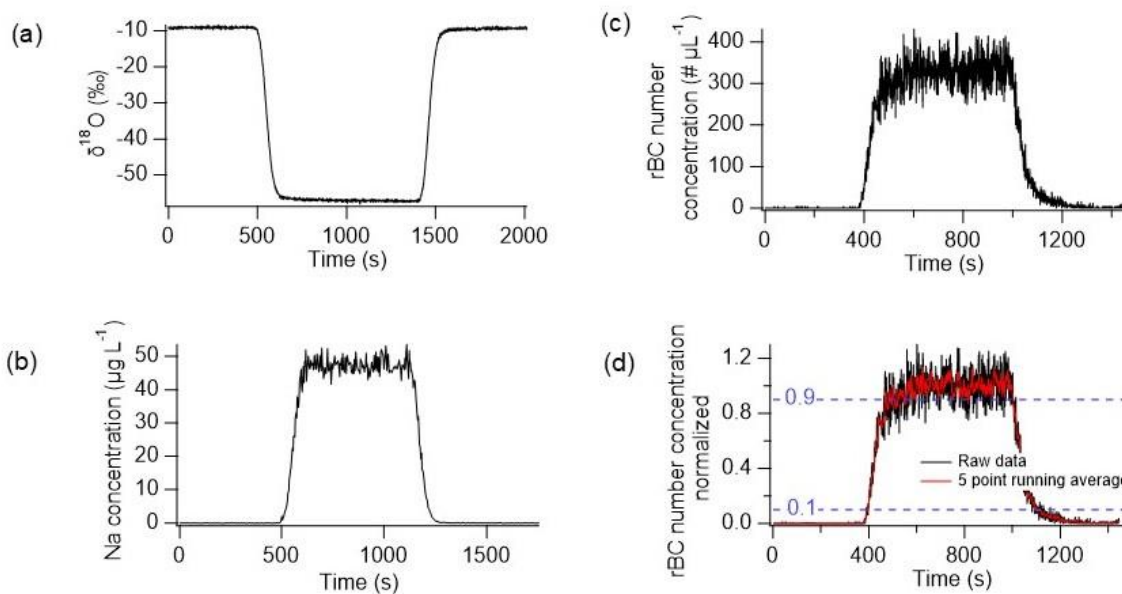


Figure 4: Results of dispersion tests: (a) $\delta^{18}\text{O}$, (b) Na concentration, (c) rBC number concentration, and (d) normalized rBC number concentration. Black and red lines represent raw data and 5 point running averages, respectively. Blue dotted lines show 0.1 and 0.9 levels.

262 sample) value, and (2) the time (t2) required for transition from 90% of the standard (or ice core/snow sample) value to 10%
 263 of the standard (or ice core/snow sample) value. The baseline was determined as the value for Milli-Q water. Response times
 264 t1 and t2 depend on how the data are smoothed owing to noise in the data signal. Table 2 shows examples of t1 and t2 when
 265 the data are smoothed by taking 5-point running means. Neither t1 nor t2 depends on the standard (or ice core/snow sample)
 266 concentrations or values (Bigler et al., 2011). For rBC, we present normalized values together with concentrations in Fig. 4 to
 267 illustrate how we determined t1 and t2. We converted t1 and t2 to depth intervals L1 and L2, respectively, assuming a constant
 268 melt speed of 30 mm s⁻¹. In Table 2, we list the averages of L1 and L2 for a rise of 10%–90% and decay of 90%–10%,
 269 respectively. L1 and/or L2 are often defined as the depth resolution of a CFA system (Bigler et al., 2011; Erhardt et al., 2023;
 270 Grieman et al., 2022). This definition gives a depth resolution of 35-40 mm for the δ¹⁸O, Na, and rBC data over the depth
 271 interval between 6.17 and 112.87 m. However, the resolution of our CFA system is better than these values suggest. We could
 272 resolve two peaks located at distances closer than the resolution defined in this way. For δ¹⁸O, Na, and rBC, peaks 10 mm
 273 apart are usually resolved, although peak heights may be slightly reduced for peaks that are less than 35-40 mm apart. For rBC
 274 and Na, L2 is slightly greater than L1, indicating that the melting direction affects the CFA signal (Breton et al., 2012). The
 275 CFA signal for rBC and Na might not be symmetrical, even if a concentration peak is symmetrical along the core depth (Breton
 276 et al., 2012). Conversely, δ¹⁸O shows similar L1 and L2 values, indicating that melting direction does not affect the CFA signal.

277 In addition to the mixing that occurs in the debubbler, valves, conductivity cells, tubing, and nebulizer systems,
 278 there is also mixing between the meltwater from the center of the ice sample and the meltwater from the ice on outside the
 279 inner wall of the melt head. However, due to the very short distance and very small dead volume within the melt head (using
 280 a 26 x 26 mm square-shaped melt head as described by Bigler et al. (2011)), this mixing is negligible compared to the
 281 mixing that occurs in other parts of the CFA system. Therefore, the signal dispersion observed in this study provides a
 282 reliable representation of the dispersion caused by the entire CFA system. Additionally, the stratigraphy of the SIGMA-D
 283 core was nearly horizontal, resulting in minimal mixing of ice from different ages.

284

285 **Table 2 Results of dispersion tests**

	University of Copenhagen type melt head	University of Maine type melt head
--	---	------------------------------------

	t1 (s)	t2 (s)	L1 (mm)	L2 (mm)	Average of L1 & L2 (mm)	t1 (s)	t2 (s)	L1 (mm)	L2 (mm)	Average of L1 & L2 (mm)
$\delta^{18}\text{O}$	78	75	39	37.5	38.3	75	81	37.5	40.5	39
rBC number concentration	67	90	33.5	45	39.3	105	124	52.5	62	57.3
Na concentration	66	74	33	37	35	57	89	28.5	44.5	36.5

286

287 3.3 Minimal losses of BC particles in the NIPR CFA system

288 Figure 5 and Table 3 present the results of rBC loss tests. The sample injected at the melt head, which then flowed through the
 289 CFA system, produced mass and number size distributions of rBC particles consistent with those derived following direct
 290 injection. The mass and number concentrations of rBC particles injected at the melt head were 94% and 102% of those
 291 determined following direct injection. Thus, the rBC concentrations of the two types of injections agreed within the bounds of

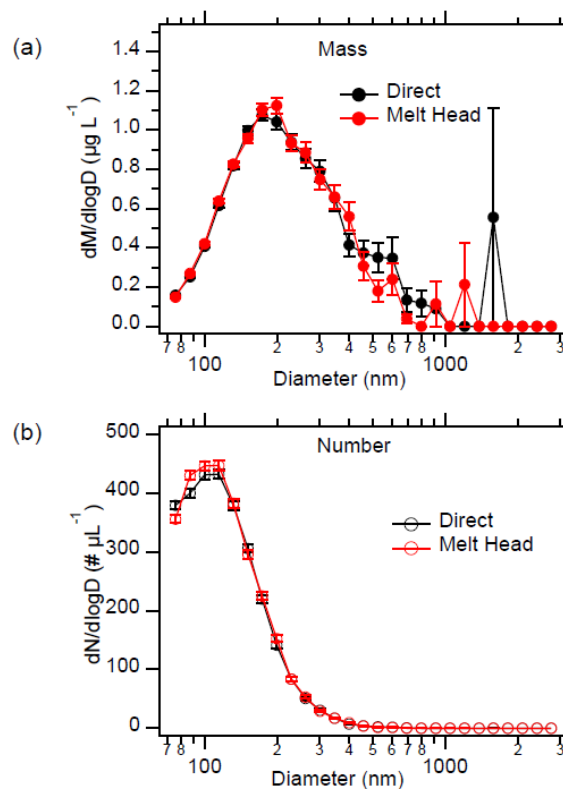


Figure 5: Comparison of direct injection of a surface snow sample collected at SIGMA-A to Marin-5 and injection at the melt head. (a) Mass and (b) number size distributions of rBC shown for direct and melt head injections. Error bars indicate $\pm 1\sigma$ of a Poisson distribution.

292 uncertainty of the BC measurements. Therefore, we can conclude that minimal loss of rBC particles occurs in the NIPR CFA
293 system. The good agreement between injection at the melt head and the direct injection also supports the reliability and
294 reproducibility of the NIPR CFA-rBC system.

295

296 **Table 3 Results of rBC loss test using a surface snow sample from SIGMA-A, northwest Greenland**

	Melt head blank	Injection at melt head	Direct injection	Ratio of injection at melt head/direct injection
rBC mass concentration ($\mu\text{g L}^{-1}$)	0.004	0.623	0.660	0.944
rBC number concentration ($\# \text{L}^{-1}$)	0.1	175.8	173.0	1.016

297

298

299 **3.4 High-resolution rBC data from the SIGMA-D ice core**

300 Figure 6 displays the raw data of BC mass and number concentrations acquired using the CFA system at 1 s interval
 301 corresponding to a depth interval of 0.0005 m, together with the 10 mm averages of the data. The ice-core chronology
 302 determined by Nagatsuka et al., (2019) with a slight modification (Goto-Azuma et al., 2024) is shown in Fig. 6. The raw mass
 303 concentration data frequently exceeded $50 \mu\text{g}\cdot\text{L}^{-1}$. However, as can be deduced from the differences in mass concentrations
 304 and number concentrations (Fig.6 (a) and (b)) and their enlarged extracts (Fig.6 (c) and (d), respectively), the sporadic high
 305 concentration peaks in the raw mass concentration data could have been formed by only a small number of large BC particles,
 306 which would result in the noise in the data. To reduce the noise, we calculated the 10 mm averages of the data, corresponding
 307 to a 1–2 week interval depending on the depth of the core. Averaging the mass concentrations over 10 mm intervals effectively
 308 filtered out data noise, while still preserving the large peaks, albeit with slightly reduced amplitudes (Fig. 6(a) and (c)). The
 309 10 mm averages of the mass concentrations often exceeded $10 \mu\text{g}\cdot\text{L}^{-1}$. The prominent peaks in mass and number concentrations

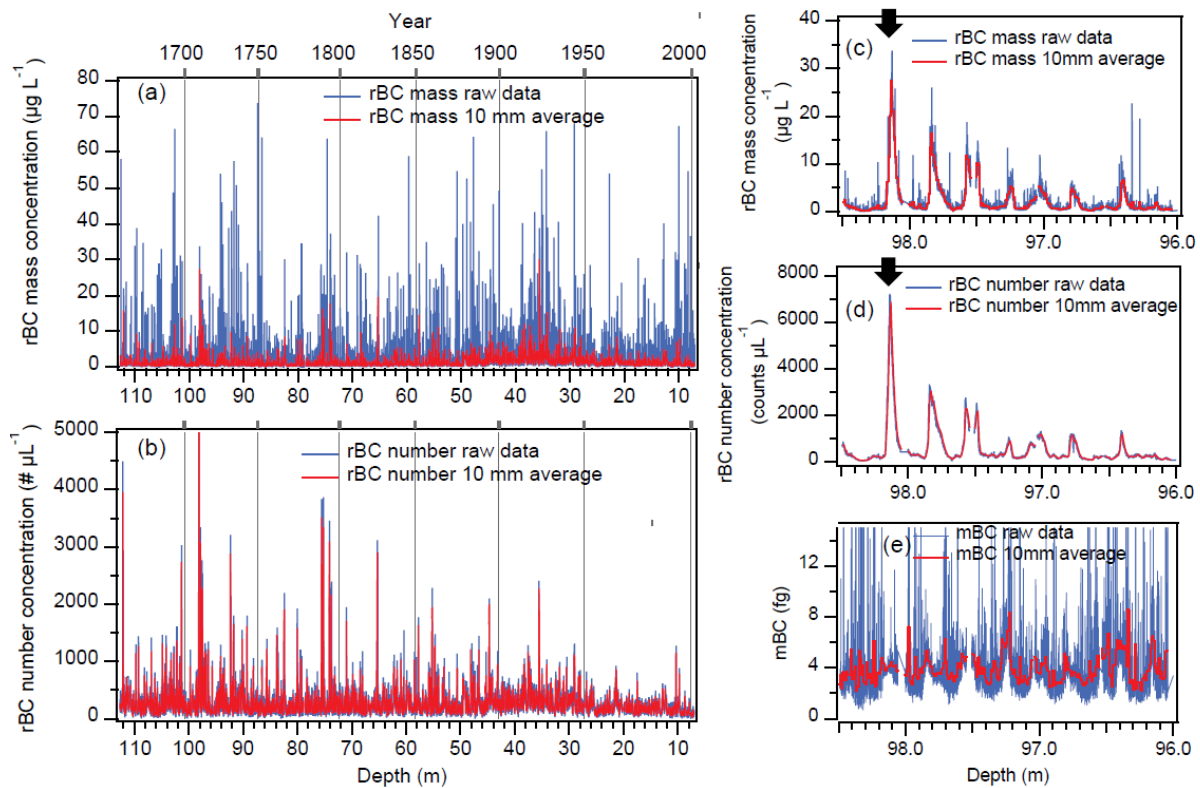
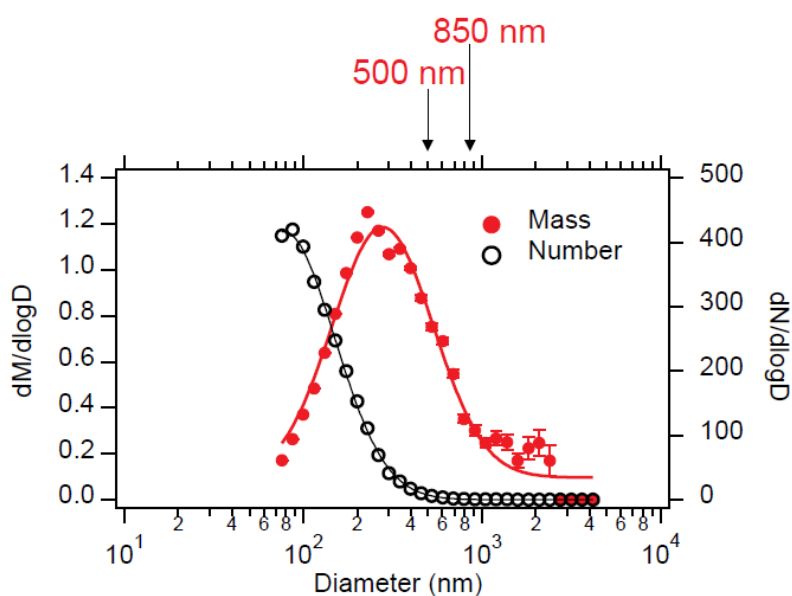


Figure 6: (a) Mass and (b) number concentrations of rBC in the SIGM-D core. (c) and (d) are enlarged extracts of (a) and (b), respectively. (e) mBC (average mass of rBC particles) for the same depth interval as (c) and (d). Raw data and 10 mm averages of the raw data are shown in blue and red, respectively. The arrows (c) and (d) denote the summer of 1710.

310 around 98.1 m correspond to the summer of 1710, when rBC particles from a significant biomass burning event were deposited
 311 at the SIGMA-D site (Goto-Azuma et al., 2024).

312 The upper limit of the measurable rBC diameters would affect the rBC mass concentrations if the ice core samples
 313 contain a large proportion of large particles. As described in Sect. 2.2, the upper limit of the NIPR rBC unit is 4 μm , whereas
 314 the upper limit of a measurement system using the off-the-shelf SP2 is 400-500 nm and that of a measurement system using
 315 an extended range SP2 and the off-the-shelf SP2-XR is 800-850 nm. If a measurement system uses a nebulizer system such as
 316 the U5000AT ultrasonic nebulizer system (Teledyne CETAC, USA), which was used in many previous studies, nebulizer
 317 efficiency is drastically reduced for diameters greater than approximately 500 nm (Mori et al., 2016), which would lead to
 318 underestimation of rBC mass concentrations if the ice core contains a large proportion of rBC particles with diameter of >500
 319 nm even if an extended range SP2 is used. We calculated the number and mass size distributions of rBC particles averaged



Ratio of rBC mass concentration	Ratio of rBC number concentration	Ratio of rBC mass concentration	Ratio of rBC number concentration
500 nm/Total	500 nm/Total	850 nm/Total	850 nm/Total
0.69	0.99	0.88	1.00

Figure 7: Averaged number (black) and mass (red) size distribution of rBC particles for the period 2003–2013, respectively. Error bars indicate $\pm 1\sigma$ of a Poisson distribution. The table shows ratios of concentrations for upper limits of 500 and 850 nm to total concentrations.

320 over different periods. As an example, the 11-year mean number and mass size distributions for 2003–2013, derived from

321 analyses of the discrete samples, are plotted in Fig. 7. It is evident from Fig. 7 that the total number concentrations of rBC
322 particles would have been affected little by the upper limits of the measurable BC diameters, which were approximately 400-
323 500 nm in previous studies and 850-900 nm if an extended range SP2 was used. In contrast, the mass concentrations would
324 have been underestimated by 31% and 12% for upper limits of 500 and 850 nm, respectively.

325 Figure 8 displays additional examples of mass size distributions of rBC particles for months with significant rBC
326 concentration peaks. Given that the upper limit of measurable rBC diameter is 500 nm, mass concentrations during the
327 summers of 1710 and 1863, and the winters of 1916/17 and 1935/36 would have been underestimated by 8, 43, 26, and 36 %,
328 respectively. The mass size distribution, and consequently the degree of underestimation, varied over time. We calculated the
329 average mass of rBC particles (mBC), by dividing the mass concentration by the number concentration, which serves as one
330 of the rBC size parameters. Fig. 6(e) illustrates an example of the mBC variability with depth, indicating seasonal changes in
331 rBC size distribution. A companion paper (Part 2, Goto-Azuma et al., 2024) further investigated the temporal variability in
332 rBC size distribution. As rBC size distribution changes over time, the underestimation ratio cannot be assumed to be constant.
333 Therefore, it is crucial to extend the measurable rBC diameters beyond 500 nm, desirably beyond 800-850 nm.

334

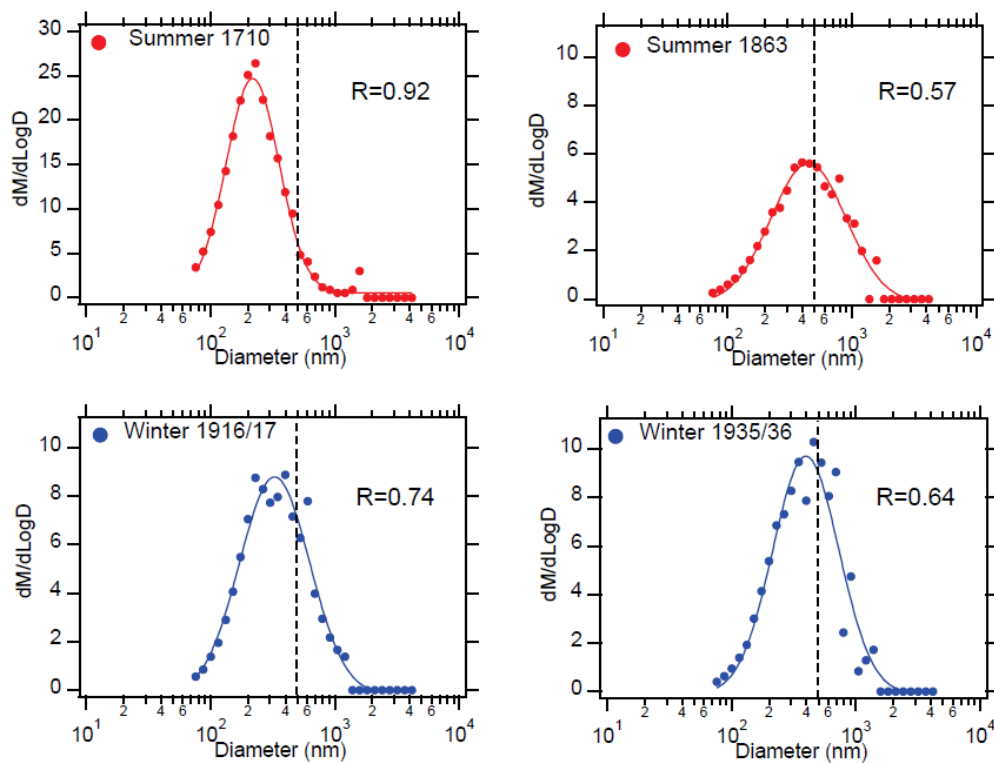


Figure 8: Examples of mass size distributions of rBC particles for summer and winter months showing high rBC concentrations. (a) Summer months of 1710, shown by the arrows in Fig. 6 (a) and (b). (b) Summer months of 1863. (c) Winter months of 1916/17. (d) Winter months of 1935/36. Summer and winter months correspond to approximately May-July and December-February, respectively (Goto-Azuma et al., 2024). The dotted lines show the upper limit of measurable rBC diameter (500 nm) for off-the-shelf SP2. R denotes the ratio of rBC mass concentration for diameter <500 nm to the total rBC mass concentration.

336 To examine the impact of large rBC particles in the SIGMA-D ice core, the rBC mass concentrations averaged for
 337 10 mm intervals, assuming different upper limits, were calculated from the size distribution data, and plotted in Fig. 9a. In Fig.
 338 9b, the ratios of the rBC mass concentrations for different upper limits versus the total rBC mass concentrations are shown.
 339 Figure 9b shows that the off-the-shelf SP2 combined with a size-independent high-efficiency nebulizer system such as the
 340 Marin-5 or the APEX-Q nebulizer systems, which would give an upper limit of 500 nm, would occasionally underestimate the
 341 rBC mass concentration by 30-40% or more. Even an extended range SP2, when combined with a size-independent high-
 342 efficiency nebulizer system, could occasionally underestimate the rBC mass concentration by 20% or more. If we use a
 343 nebulizer system such as the U5000AT, underestimation would be even greater, though difficult to quantify due to its size-

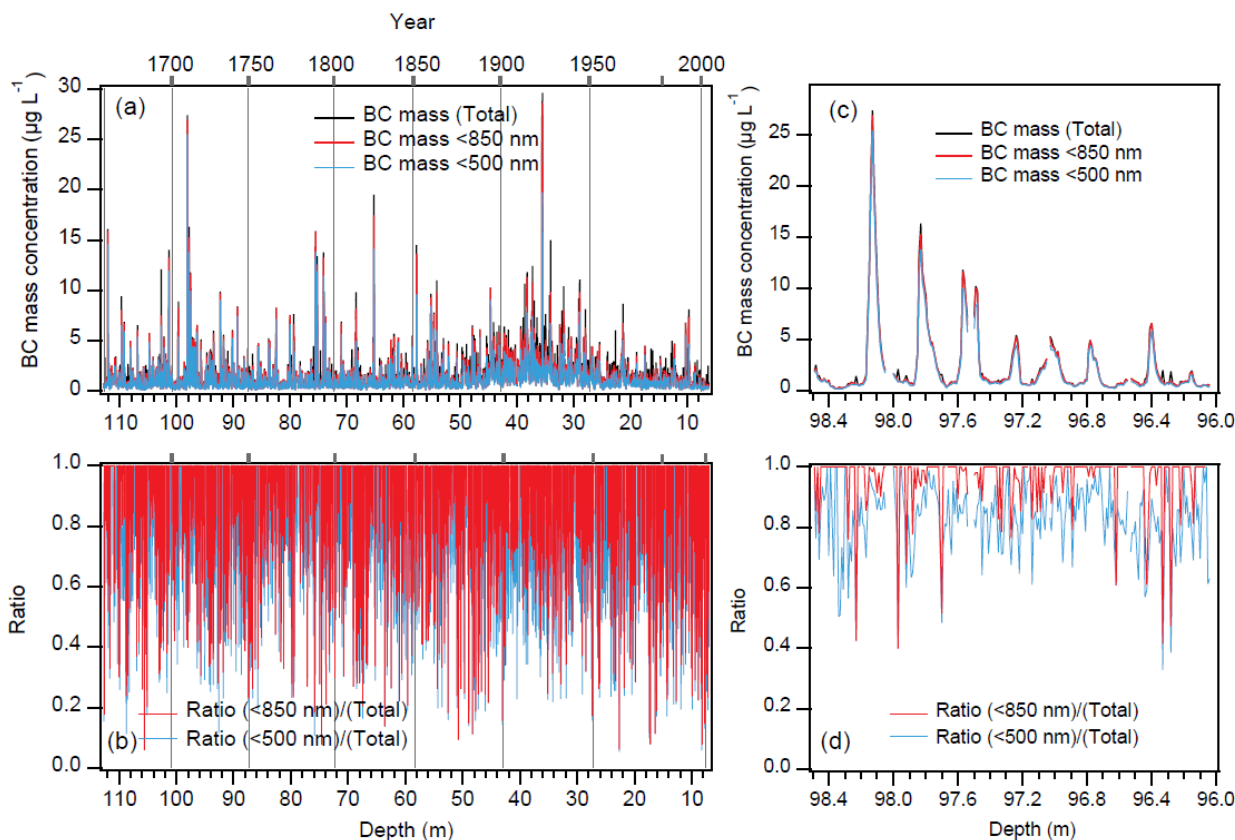


Figure 9: Comparison of rBC mass concentration (10 mm averages) in the SIGMA-D core for different upper limits of measurable rBC diameters. (a) Total concentration measured in this study (upper limit: 4 µm), concentration for upper limit of 850 nm, and concentration for upper limit of 500 nm are displayed in black, red, and blue colors, respectively. (b) Ratio of rBC mass concentration for upper limit of 850 nm (red) and 500 nm (blue) to total concentration. (c) and (d) are enlarged extracts of (a) and (b), respectively.

344 and time- dependent efficiency. Figure 10 presents histograms of the ratios of rBC mass concentrations for upper limits of 500
 345 and 850 nm. For the upper limit of 500 nm, 67% of the 10 mm averages account for <90% of the total rBC mass concentrations;
 346 whereas for the upper limit of 850 nm, 15% of the 10 mm averages account for <90% of the total rBC mass concentrations.

347
 348
 349
 350

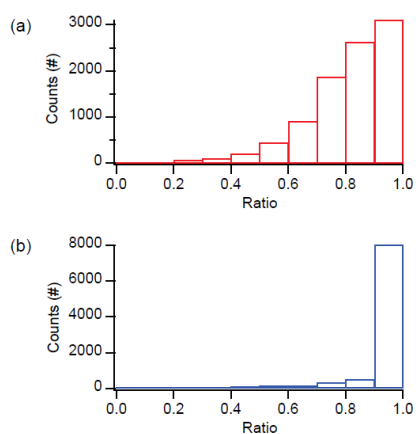


Figure 10: Histograms of underestimation for 10 mm averaged data. Horizontal axis represents the ratio of mass concentration for an upper limit of (a) 500 nm and (b) 850 nm. Vertical axis represents the number of 10 mm averaged data in each ratio bin.

351

352 4. Conclusions

353 We developed a CFA system and incorporated an rBC unit that uses the improved rBC measurement technique developed by
 354 Mori et al. (2016). The CFA system can acquire continuous and high-resolution measurements of the number and mass
 355 concentrations of rBC, and the size distribution of rBC particles, in addition to stable water isotopes ($\delta^{18}\text{O}$ and δD), six elements
 356 (^{23}Na , ^{24}Mg , ^{27}Al , ^{39}K , ^{43}Ca , and ^{56}Fe), microparticles, electrical conductivity, and methane. There were minimal losses of rBC
 357 particles within the NIPR CFA system. We analysed the SIGMA-D ice core retrieved from northwest Greenland using this
 358 newly developed system. If we define the depth resolution as the average of the rise of 10%–90% and decay of 90%–10% of
 359 the CFA signal, the resolutions were 38, 39, and 35 mm for $\delta^{18}\text{O}$, rBC, and Na, respectively. These depth resolutions correspond
 360 to the temporal resolutions of 0.08–0.16, 0.11–0.23, and 0.07–0.15 years for $\delta^{18}\text{O}$, rBC, and Na, respectively, depending on
 361 depth. However, we could usually resolve two peaks that were approximately 10 mm apart, corresponding to 1-2 weeks
 362 depending on depth. We were able to analyse monthly resolved rBC data as described in the companion paper, i.e., Part 2 of
 363 our study on rBC in the SIGMA-D core (Goto-Azuma et al., 2024).

364 The Wide-Range SP2 and the Marin-5 nebulizer system allowed analysis of rBC particles with diameter between
 365 approximately 70 nm and 4 μm , contrasting with the analysis of rBC particles with diameter of between 70 and 400-500 nm
 366 reported in previous ice-core studies. This enabled us to reconstruct accurate mass concentrations and size distributions of rBC
 367 particles, together with their temporal changes (Goto-Azuma et al., 2024), which could contribute to estimation of the impacts

368 of rBC on the radiation budget and cloud microphysics. Using the size distribution data, we estimated the extent of
369 underestimation that would result from using (1) an off-the-shelf traditional SP2, which can measure rBC particles with
370 diameters <500nm., and (2) an SP2 modified by Moteki and Kondo (2011) or an off-the-shelf SP2-XR which can measure
371 rBC particles with diameter <850 nm. In both cases, we assumed size-independent efficiency for nebulizer systems such as
372 the Marin-5 and the APEX-Q. For (1), approximately 67% and 37 % of the 10 mm averaged data from the SIGMA-D core
373 accounted for <90% and <80% of the total rBC mass concentrations, respectively. For (2), approximately 15% and 10% of the
374 10 mm averaged data from the SIGMA-D core accounted for <90% and <80% of the total rBC mass concentrations,
375 respectively. The extent of the underestimation depends on depth and thus on the age of the core. For the period 2003–2013,
376 (1) and (2) would lead to underestimation of the averaged mass concentration by 31% and 12%, respectively. For large
377 concentration peaks resulting from significant boreal forest fires and anthropogenic inputs, underestimation would frequently
378 exceed 40%.

379 Although few ice core studies have considered the size distribution of rBC and estimated the extent of underestimation
380 of rBC mass concentrations, the present-day snow from Svalbard (Mori et al., 2019) and an ice core from Mt. Elbrus in the
381 western Caucasus Mountains (Lim et al., 2017) do contain non-negligible amounts of rBC particles with diameter of >500 nm
382 or 850 nm. Since the size distributions do not always follow the lognormal distributions, the improved method for accurate
383 measurement of rBC mass concentrations should be employed to properly constrain aerosol models.

384

385 **Appendix A: Details of the NIPR CFA system**

386 An ice core sample (cross section: 34 mm × 34 mm, length: ~0.5 m) was placed on a melt head inside a freezer. An 850 g
387 weight was placed on top of the ice sample to allow stable melting. Before the ice core sample was completely melted, another
388 similarly sized ice core sample was stacked on top of the first sample to maintain continuous melting of the ice samples. To
389 promote melting, heaters are inserted into the melt head (Bigler et al., 2011; Osterberg et al., 2006). In the earlier NIPR CFA
390 system, we used a melt head developed at the University of Maine (Osterberg et al., 2006). However, in this study, we used a
391 melt head similar to the one developed at the University of Copenhagen by Bigler et al. (2011) for the depth interval between
392 11.3 and 112.8 m of the SIGMA-D core. The University of Maine type melt head, designed principally for use in firn core
393 analyses, is not airtight. For methane analysis, we had to use an airtight melt head such as the one used by Bigler et al. (2011).
394 For the depth interval between 6.17 and 11.3 m of the SIGMA-D core, we used the University of Maine type melt head

395 (Dallmayr et al., 2016; Osterberg et al., 2006) to reduce water percolation through the porous firn caused by capillary action
396 (Osterberg et al., 2006). For depths < 49.3 m, methane measurement was not performed.

397 The depth of an ice core sample was assigned using a laser positioning sensor (LKG-G505, Keyence, Japan), which
398 determined the distance from the sensor to the top of the weight (Dallmayr et al., 2016). A typical melt speed, regulated by the
399 voltage applied to the heaters in the melt head, was 30 mm min⁻¹. The depth resolution of the laser positioning sensor with this
400 melt speed was approximately 0.3 ± 0.1 mm. The meltwater collected in the contamination-free inner part of the melt head is
401 drawn through perfluoroalkoxy alkane tubing, an injection valve, and the debubbler unit by a peristaltic pump (Minipuls3 MP-
402 2, Gilson, USA). Following removal of air bubbles by the debubbler unit, the meltwater is introduced to the different
403 measurement units and to the fraction collector unit using peristaltic pumps (Reglo Digital ISM596, ISMATEC, Germany).
404 Before each unit, an electrical conductivity cell (conductivity meter Model 1056, Amber Science Inc., USA) is placed as close
405 as possible to the unit to synchronise the depths of the ice core data acquired by the different measurement units and the depths
406 of the meltwater samples collected by the fraction collector unit (McConnell et al., 2002; Dallmayr et al., 2016). A length of
407 approximately 7 m of the ice core was melted once or twice a week. The lengths of the tubing between (1) the melt head and
408 the debubbler, (2) the debubbler and the ICP-MS unit, (3) the debubbler and the water isotope unit, and (4) the debubbler and
409 the rBC unit were approximately 1 m, 3 m, 1.2 m, and 1.5m, respectively. The inner diameters of the tubing for the ICP-MS
410 unit, water isotope unit, and rBC unit were 0.03, 0.02, and 0.03 inches, respectively.

411 The ICP-MS unit consists of an ICP-MS (7700 ICP-MS, Agilent Technologies, USA) including a nebulizer system.
412 The elements ²³Na, ²⁴Mg, ²⁷Al, ³⁹K, ⁴³Ca, and ⁵⁶Fe were each measured at a 3.00 s interval. Additionally, ⁸⁹Y was measured
413 at a 3.00 s interval to check the stability of the ICP-MS. Data acquisition times for ²³Na, ²⁴Mg, ²⁷Al, ³⁹K, ⁴³Ca, ⁵⁶Fe, and ⁸⁹Y
414 were 0.02, 0.1, 0.2, 0.1, 2.27, 0.252, and 0.044 s, respectively. We used mainly ²³Na data to date the core. The concentration
415 of each of the elements was calibrated both before and after the CFA measurements of the day using a multi-element standard
416 solution (XSTC-331, Spex CertiPrep, USA) diluted with ultra-pure water (Milli-Q water, Milli-Q Advantage, Merck
417 Millipore, Germany). The detection limit, defined as [3σ of the blank value + the intercept of the calibration line], of ²³Na
418 is 0.5 µg L⁻¹.

419 The stable water isotope unit is essentially same as that used by Dallmayr et al. (2016). It consists of a vaporization
420 module (Gkinis et al., 2011; Dallmayr et al., 2016), and a wavelength-scanned cavity ring-down spectrometer (L2130-i or
421 L2120-i, Picarro Inc., USA). The Picarro L2130-i was used for the depth interval between 107.3 and 49.3 m, while the

422 Picarro L2120-I was used for the remaining depths. We calibrated the spectrometer by analysing three sets of laboratory
423 water isotope standards after the CFA measurements of the day. These laboratory standards were calibrated with VSMOW2
424 and SLAP2 standards purchased from the International Atomic Energy Agency. Details of calibrations and the performance
425 of the stable water isotope unit have been described in a previous study (Dallmayr et al., 2016). Both the L2130-i and L2120-
426 i demonstrated sufficient stability during the 4-5 hours of a daily CFA session, confirmed by Mill-Q water runs before and
427 after the CFA measurements. The good agreement between the CFA data (from Section A of the SIGMA-D core) and
428 discrete sample data (from Section B of the core) also confirms the stability of both Picarras (Goto-Azuma et al., 2024).

429

430 **Appendix B: Analyses of discrete samples**

431 **B1 Discrete samples from Section A of SIGMA-D core**

432 From the top 6.17 m of Section A of the SIGMA-D core, discrete samples were prepared (Sect. 2.4). The samples in glass
433 bottles were analysed for stable isotopes of water using a near-infrared cavity ring-down spectrometer (L2120-i, Picarro, Inc.
434 USA), a high-precision vaporizer (A0211, Picarro Inc., USA), and an autosampler (PAL HTC9 - xt - LEAP, LEAP
435 Technologies, USA). The precision of determination was $\pm 0.05\%$ for $\delta^{18}\text{O}$. The samples in polypropylene bottles were
436 analysed for six elements (^{23}Na , ^{24}Mg , ^{27}Al , ^{39}K , ^{40}Ca , and ^{56}Fe) with an ICP-MS (7700 ICP-MS, Agilent Technologies, USA)
437 in a class 10,000 clean room at NIPR.

438

439 **B2 Discrete samples from Section B of SIGMA-D core**

440 Samples from depths above 61.2 m were analysed for Na^+ , K^+ , Mg^{2+} and Ca^{2+} , Cl^- , NO_3^- , and SO_4^{2-} with two ion
441 chromatographs (ICS-2100, Thermo Fisher Scientific, USA) at Hokkaido University, Japan, whereas samples from depths
442 between 61.2 and 112.87 m were analysed for NH_4^+ , Na^+ , K^+ , Mg^{2+} , Ca^{2+} , Cl^- , NO_3^- , and SO_4^{2-} with two ion chromatographs
443 (ICS-2000, Thermo Fisher Scientific, USA) at NIPR. The limit of detection of Na^+ measured at Hokkaido University was 10
444 $\mu\text{g}\cdot\text{L}^{-1}$, and that measured at NIPR was 0.2 $\mu\text{g}\cdot\text{L}^{-1}$. Stable water isotopes were analysed for all samples from Section B using
445 a near-infrared cavity ring-down spectrometer (L2130-i, Picarro Inc., USA) and a high-throughput vaporizer (A0212, Picarro
446 Inc., USA) at Hokkaido University. The precision of determination was $\pm 0.1\%$ for $\delta^{18}\text{O}$. The good agreement between the
447 CFA data and discrete sample data from Sections A and B, respectively, ensured the high quality of the CFA data. For dating
448 purposes, tritium concentrations were measured using a liquid scintillation counter (LSC-LB3; Aloka Co. Ltd., Japan) at 0.05

449 m intervals for the depth interval of 19.15–26.47 m (Nagatsuka et al., 2021).

450

451 **Appendix C**

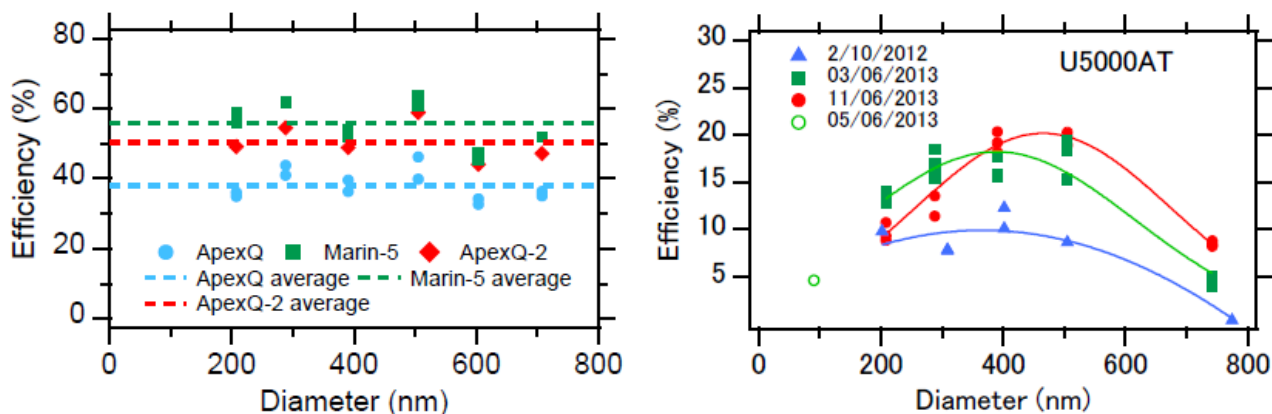


Figure C1: (a) Comparison of Marin-5 and APEX-Q nebulizer efficiency for a flow rate of 0.19 mL min^{-1} . A MicroMist U-series AR30-1-UM05E (Glass Expansion, Australia) was used for the Marin-5 nebulizer system. On the other hand, two types of nebulizers, a Conikal Nebulizer AR30-1-FC1ES (Glass Expansion, Australia) and a MicroMist U-Series nebulizer AR30-1-UM05E (Glass Expansion, Australia) were used for the Apex-Q nebulizer system. ApexQ and ApexQ2 represent the APEX-Q nebulizer system used with the former and the latter nebulizers, respectively. (b) Repeated measurements of efficiency of U5000AT nebulizer system for a flow rate of 0.19 mL min^{-1} .

452 **Data availability**

453 The data used in this study will be submitted to the Arctic Data Archive System when the manuscript has been published.

454

455 **Author contributions**

456 KGA designed the study and led the manuscript writing. RD, MH, KGA, and KeK built the CFA system at NIPR. NM, TM, SO, YK, and MK developed the improved method for rBC analyses, including the calibration method. YOT, RD, JO, and KyK performed the CFA analyses of the SIGMA-D core. YOT measured nebulizer efficiencies and performed rBC loss tests. YOT, JO and MH performed dispersion tests. SM, KoF, NN, and AT dated the core. KGA, YOT, and KaF analysed the CFA data. MH and SM measured ion concentrations. TA designed and led the ice coring project at SIGMA-D. All the authors discussed the results.

462

463 **Competing interests**

464 The authors declare that they have no conflict of interest.

465

466 **Acknowledgements**

467 We would like to thank Hideaki Motoyama for drilling the SIGMA-D core and Yuki Komuro for cutting and processing the
468 core in the field. We also express our gratitude to Kazuhiro Hayashi for assisting with the dispersion tests. We are grateful to
469 the University of Copenhagen and the University of Maine for providing the melt head designs. We acknowledge Margit
470 Schwikowski and Joe McConnell for their valuable advice in developing the CFA-rBC system at NIPR. Additionally, we
471 appreciate the helpful comments from the three anonymous reviewers. This study has been supported by the JSPS KAKENHI
472 (Grant Numbers: JP 22221002, JP23221004, and JP18H04140), the Arctic Challenge for Sustainability (ArCS) Project
473 (Program Grant Number: JPMXD130000000)), the Arctic Challenge for Sustainability II (ArCS II) Project (Program Grant
474 Number: JPMXD1420318865), and the Environment Research and Technology Development Funds (JPMEERF20172003,
475 JPMEERF20202003 and JPMEERF20232001) of the Environmental Restoration and Conservation Agency of Japan.

476 **References**

- 477 AMAP: Arctic Climate Change Update 2021: Key Trends and Impacts, Summary for Policy-makers, 2021.
- 478 Arienzo, M. M., McConnell, J. R., Murphy, L. N., Chellman, N., Das S., Kipfstuhl, S., and Mulvaney, R.: Holocene black
479 carbon in Antarctica paralleled Southern Hemisphere climate, *J. Geophys. Res.-Atmos.*, 122, 6713 - 6728,
480 doi:10.1002/2017JD026599, 2019.
- 481 Baumgardner, D.: Warming of the Arctic lower stratosphere by light absorbing particles, *Geophys. Res. Lett.*, 31,
482 10.1029/2003gl018883, 2004.
- 483 Baumgardner, D., Kok, G., and Raga, G.: Warming of the Arctic lower stratosphere by light absorbing particles, *Geophys.*
484 *Res. Lett.*, 31, <https://doi.org/10.1029/2003GL018883>, 2004.
- 485 Bigler, M., Svensson, A., Kettner, E., Vallelonga, P., Nielsen, M. E., and Steffensen, J. P.: Optimization of high-resolution
486 continuous flow analysis for transient climate signals in ice cores, *Environ. Sci. Technol.*, 45, 4483–4489,
487 10.1021/es200118j, 2011.

488 Bisiaux, M. M., Edwards, R., McConnell, J. R., Albert, M. R., Anshütz, H., Neumann, T. A., Isaksson, E., and Penner, J. E.:
489 Variability of black carbon deposition to the East Antarctic Plateau, 1800–2000 AD, *Atmos. Chem. Phys.*, 12, 3799–3808,
490 10.5194/acp-12-3799-2012, 2012a.

491 Bisiaux, M. M., Edwards, R., McConnell, J. R., Curran, M. A. J., Van Ommen, T. D., Smith, A. M., Neumann, T. A., Pasteris,
492 D. R., Penner, J. E., and Taylor, K.: Changes in black carbon deposition to Antarctica from two high-resolution ice core
493 records, 1850–2000 AD, *Atmos. Chem. Phys.*, 12, 4107–4115, 10.5194/acp-12-4107-2012, 2012b.

494 Bond, T. C., Doherty, S. J., Fahey, D. W., Forster, P. M., Berntsen, T., DeAngelo, B. J., Flanner, M. G., Ghan, S., Kärcher, B.,
495 Koch, D., Kinne, S., Kondo, Y., Quinn, P. K., Sarofim, M. C., Schultz, M. G., Schulz, M., Venkataraman, C., Zhang, H.,
496 Zhang, S., Bellouin, N., Guttikunda, S. K., Hopke, P. K., Jacobson, M. Z., Kaiser, J. W., Klimont, Z., Lohmann, U., Schwarz,
497 J. P., Shindell, D., Storelvmo, T., Warren, S. G., and Zender, C. S.: Bounding the role of black carbon in the climate system:
498 A scientific assessment, *J. Geophys. Res.-Atmos.*, n/a-n/a, 10.1002/jgrd.50171, 2013.

499 Breton, D. J., Koffman, B. G., Kurbatov, A. V., Kreutz, K. J., and Hamilton, G. S.: Quantifying signal dispersion in a hybrid
500 ice core melting system, *Environ. Sci. Technol.*, 46, 11922–11928, 10.1021/es302041k, 2012.

501 Dallmayr, R., Goto-Azuma, K., Kjær, H. A., Azuma, N., Takata, M., Schüpbach, S., and Hirabayashi, M.: A high-resolution
502 continuous flow analysis system for polar ice cores, *B. Glaciol. Res.*, 34, 11–20, 10.5331/bgr.16R03, 2016.

503 Dibb, J. E., Whitlow, S. I., and Arsenault, M.: Seasonal variations in the soluble ion content of snow at Summit, Greenland:
504 Constraints from three years of daily surface snow samples, *Atmos. Environ.*, 41, 5007–5019,
505 10.1016/j.atmosenv.2006.12.010, 2007.

506 Du, Z.-H., Xiao, C.-D., Dou, T.-F., Li, C.-J., Ding, M.-H., Sharma, S., Ma, X.-Y., Wang, S.-M., and Zhang, W.-B.: A shallow
507 ice core from East Greenland showing a reduction in black carbon during 1990–2016, *Adv. Clim. Change Res.*, 11, 360–
508 369, <https://doi.org/10.1016/j.accre.2020.11.009>, 2020.

509 Erhardt, T., Jensen, C. M., Adolphi, F., Kjær, H. A., Dallmayr, R., Twarloh, B., Behrens, M., Hirabayashi, M., Fukuda, K.,
510 Ogata, J., Burgay, F., Scoto, F., Crotti, I., Spagnesi, A., Maffezzoli, N., Segato, D., Paleari, C., Mekhaldi, F., Muscheler, R.,
511 Darfeuille, S., and Fischer, H.: High-resolution aerosol data from the top 3.8-kyr of the East Greenland Ice coring Project
512 (EGRIP) ice core, *Earth Syst. Sci. Data*, 15, 5079–5091, 10.5194/essd-15-5079-2023, 2023.

513 Gkinis, V., Popp, T. J., Blunier, T., Bigler, M., Schupbach, S., Kettner, E., and Johnsen, S. J.: Water isotopic ratios from a
514 continuously melted ice core sample, *Atmos. Meas. Tech.*, 4, 2531–2542, 10.5194/amt-4-2531-2011, 2011.

515 Goto-Azuma, K., Ogawa-Tsukagawa, Y., Fukuda, K., Fujita, K., Hirabayashi, M., Dallmayr, R., Ogata, J., Moteki, N., Mori,
516 T., Ohata, S., Kondo, Y., Koike⁶, M., Matoba, S., and Aoki, T.: High-resolution analyses of concentrations and sizes of
517 black carbon particles deposited on northwest Greenland over the past 350 years - Part 2: Seasonal and temporal trends in
518 black carbon originated from fossil fuel combustion and biomass burning, *EGUsphere*, [https://doi.org/10.5194/egusphere-](https://doi.org/10.5194/egusphere-2024-1498)
519 [2024-1498](https://doi.org/10.5194/egusphere-2024-1498), 2024.

520 Grieman, M. M., Hoffmann, H. M., Humby, J. D., Mulvaney, R., Nehrbass-Ahles, C., Rix, J., Thomas, E. R., Tuckwell, R.,
521 and Wolff, E. W.: Continuous flow analysis methods for sodium, magnesium, and calcium detection in the Skytrain ice core,
522 *J. Glaciol.*, 68, 90–100, [10.1017/jog.2021.75](https://doi.org/10.1017/jog.2021.75), 2022.

523 Kaspari, S. D., Schwikowski, M., Gysel, M., Flanner, M. G., Kang, S., Hou, S., and Mayewski, P. A.: Recent increase in black
524 carbon concentrations from a Mt. Everest ice core spanning 1860–2000 AD, *Geophys. Res. Lett.*, 38, L04703,
525 [10.1029/2010gl046096](https://doi.org/10.1029/2010gl046096), 2011.

526

527 Kinase, T., Adachi, K., Oshima, N., Goto-Azuma, K., Ogawa-Tsukagawa, Y., Kondo, Y., Moteki, N., Ohata, S., Mori, T.,
528 Hayashi, M., Hara, K., Kawashima, J., and Kita, K.: Concentrations and size distributions of black carbon in the surface
529 snow of Eastern Antarctica in 2011. *J. Geophys. Res.-Atmos.*, 125, e2019JD030737. <https://doi.org/10.1029/2019JD030737>,
530 2020. Kuramoto, T., Goto-Azuma, K., Hirabayashi, M., Miyake, T., Motoyama, H., Dahl-Jensen, D., and Steffensen, J. P.:
531 Seasonal variations of snow chemistry at NEEM, Greenland, *Ann. Glaciol.*, 52, 193–200, [10.3189/172756411797252365](https://doi.org/10.3189/172756411797252365),
532 2011.

533 Lim, S., Fain, X., Zanatta, M., Cozic, J., Jaffrezo, J.-L., Ginot, P., and Laj, P.: Refractory black carbon mass concentrations
534 in snow and ice: method evaluation and inter-comparison with elemental carbon measurement, *Atmos. Meas. Tech.*, 7,
535 3307-3324. doi: [10.5194/amt-7-3307-2014](https://doi.org/10.5194/amt-7-3307-2014), 2014.

536 Lim, S., Fain, X., Ginot, P., Mikhalenko, V., Kutuzov, S., Paris, J. D., Kozachek, A., and Laj, P.: Black carbon variability
537 since preindustrial times in the eastern part of Europe reconstructed from Mt. Elbrus, Caucasus, ice cores, *Atmos. Chem.*
538 *Phys.*, 17, 3489–3505, [10.5194/acp-17-3489-2017](https://doi.org/10.5194/acp-17-3489-2017), 2017.

539 Matoba, S., Motoyama, H., Fujita, K., Yamasaki, T., Minowa, M., Onuma, Y., Komuro, Y., Aoki, T., Yamaguchi, S.,
540 Sugiyama, S., and Enomoto, H.: Glaciological and meteorological observations at the SIGMA-D site, northwestern
541 Greenland Ice Sheet, *B. Glaciol. Res.*, 33, 7-14, [10.5331/bgr.33.7](https://doi.org/10.5331/bgr.33.7), 2015.

542 Matoba, S., Niwano, M., Tanikawa, T., Iizuka, Y., Yamasaki, T., Kurosaki, Y., Aoki, T., Hashimoto, A., Hosaka, M., and
543 Sugiyama, S.: Field activities at the SIGMA-A site, northwestern Greenland Ice Sheet, 2017, *B. Glaciol. Res.*, 36, 15–22,
544 10.5331/bgr.18R01, 2018.

545 Matsui, H.: Development of a global aerosol model using a two-dimensional sectional method: 1. Model design, *J. Adv. Model.*
546 *Earth Syst.*, 9, 1921–1947, doi:10.1002/2017MS000936, 2017.

547 Matsui, H. and Mahowald, N.: Development of a global aerosol model using a two-dimensional sectional method: 2.
548 Evaluation and sensitivity simulations, *J. Adv. Model. Earth Syst.*, 9, 1887–1920, doi:10.1002/2017MS000937, 2017.

549 Matsui, H., Mori, T., Ohata, S., Moteki, N., Oshima, N., Goto-Azuma, K., Koike, M., and Kondo, Y.: Contrasting source
550 contributions of Arctic black carbon to atmospheric concentrations, deposition flux, and atmospheric and snow radiative
551 effects, *Atmos. Chem. Phys.*, 22, 8989–9009, 10.5194/acp-22-8989-2022, 2022.

552 McConnell, J. R., Lamorey, G. W., Lambert, S. W., and Taylor, K. C.: Continuous ice-core chemical analyses using inductively
553 coupled plasma mass spectrometry, *Environ. Sci. Technol.*, 36, 7–11, 10.1021/es011088z, 2002.

554 McConnell, J. R., Edwards, R., Kok, G. L., Flanner, M. G., Zender, C. S., Saltzman, E. S., Banta, J. R., Pasteris, D. R., Carter,
555 M. M., and Kahl, J. D.: 20th-century industrial black carbon emissions altered Arctic climate forcing, *Science*, 317, 1381–
556 1384, 10.1126/science.1144856, 2007.

557 Mori, T., Moteki, N., Ohata, S., Koike, M., Goto-Azuma, K., Miyazaki, Y., and Kondo, Y.: Improved technique for measuring
558 the size distribution of black carbon particles in liquid water, *Aerosol Sci. Tech.*, 50, 242–254,
559 10.1080/02786826.2016.1147644, 2016.

560 Mori, T., Goto-Azuma, K., Kondo, Y., Ogawa-Tsukagawa, Y., Miura, K., Hirabayashi, M., Oshima, N., Koike, M., Kupiainen,
561 K., Moteki, N., Ohata, S., Sinha, P. R., Sugiura, K., Aoki, T., Schneebeli, M., Steffen, K., Sato, A., Tsushima, A., Makarov,
562 V., Omiya, S., Sugimoto, A., Takano, S., and Nagatsuka, N.: Black carbon and inorganic aerosols in Arctic snowpack, *J.*
563 *Geophys. Res.-Atmos.*, 124, 13325–13356, 10.1029/2019jd030623, 2019.

564 Mori, T., Kondo, Y., Ohata, S., Goto-Azuma, K., Fukuda, K., Ogawa-Tsukagawa, Y., Moteki, N., Yoshida, A., Koike, M.,
565 Sinha, P. R., Oshima, N., Matsui, H., Tobo, Y., Yabuki, M., and Aas, W.: Seasonal variation of wet deposition of black
566 carbon at Ny-Ålesund, Svalbard, *J. Geophys. Res.-Atmos.*, 126, e2020JD034110, <https://doi.org/10.1029/2020JD034110>,
567 2021.

568 Moteki, N.: Climate-relevant properties of black carbon aerosols revealed by in situ measurements: a review, *Prog. Earth*
569 *Planet. Sci.*, 10, 12, 10.1186/s40645-023-00544-4, 2023.

570 Moteki, N. and Kondo, Y.: Dependence of laser-induced incandescence on physical properties of black carbon aerosols:
571 Measurements and theoretical interpretation, *Aerosol Sci. Tech.*, 44, 663–675, 10.1080/02786826.2010.484450, 2010.

572 Nagatsuka, N., Goto-Azuma, K., Tsushima, A., Fujita, K., Matoba, S., Onuma, Y., Dallmayr, R., Kadota, M., Hirabayashi, M.,
573 Ogata, J., Ogawa-Tsukagawa, Y., Kitamura, K., Minowa, M., Komuro, Y., Motoyama, H., and Aoki, T.: Variations in
574 mineralogy of dust in an ice core obtained from northwestern Greenland over the past 100 years, *Clim. Past*, 17, 1341–1362,
575 10.5194/cp-17-1341-2021, 2021.

576 Nakazawa, F., Nagatsuka, N., Hirabayashi, M., Goto-Azuma, K., Steffensen, J. P., and Dahl-Jensen, D.: Variation in recent
577 annual snow deposition and seasonality of snow chemistry at the east Greenland ice core project (EGRIP) camp, Greenland,
578 *Polar Sci.*, 27, 100597, <https://doi.org/10.1016/j.polar.2020.100597>, 2021.

579 Ohata, S., Moteki, N., and Kondo, Y.: Evaluation of a method for measurement of the concentration and size distribution of
580 black carbon particles suspended in rainwater, *Aerosol Sci. Tech.*, 45, 1326–1336, 10.1080/02786826.2011.593590, 2011.

581 Ohata, S., Moteki, N., Schwarz, J., Fahey, D., and Kondo, Y.: Evaluation of a method to measure black carbon particles
582 suspended in rainwater and snow samples, *Aerosol Sci. Technol.*, 47, 1073–1082, 10.1080/02786826.2013.824067, 2013.

583 Osmont, D., Wendl, I. A., Schmidely, L., Sigl, M., Vega, C. P., Isaksson, E., and Schwikowski, M.: An 800-year high-
584 resolution black carbon ice core record from Lomonosovfonna, Svalbard, *Atmos. Chem. Phys.*, 18, 12777–12795,
585 10.5194/acp-18-12777-2018, 2018.

586 Osterberg, E. C., Handley, M. J., Sneed, S. B., Mayewski, P. A., and Kreutz, K. J.: Continuous ice core melter system with
587 discrete sampling for major ion, trace element, and stable isotope analyses, *Environ. Sci. Technol.*, 40, 3355–3361,
588 10.1021/es052536w, 2006.

589 Petzold, A., Ogren, J. A., Fiebig, M., Laj, P., Li, S.-M., Baltensperger, U., Holzner-Popp, T., Kinne, S., Pappalardo, G.,
590 Sugimoto, N., Wehrli, C., Wiedensohler, A., and Zhang, X.-Y.: Recommendations for reporting “black carbon”
591 measurements, *Atmos. Chem. Phys.*, 13, 8365–8379, 10.5194/acp-13-8365-2013, 2013.

592 Rantanen, M., Karpechko, A. Y., Lipponen, A., Nordling, K., Hyvärinen, O., Ruosteenoja, K., Vihma, T., and Laaksonen, A.:
593 The Arctic has warmed nearly four times faster than the globe since 1979, *Commun. Earth Environ.*, 3, 168, 10.1038/s43247-
594 022-00498-3, 2022.

595 Schwarz, J. P., Gao, R. S., Fahey, D. W., Thomson, D. S., Watts, L. A., Wilson, J. C., Reeves, J. M., Darbeheshti, M.,
596 Baumgardner, D. G., Kok, G. L., Chung, S. H., Schulz, M., Hendricks, J., Lauer, A., Kärcher, B., Slowik, J. G., Rosenlof,
597 K. H., Thompson, T. L., Langford, A. O., Loewenstein, M., and Aikin, K. C.: Single-particle measurements of mid-latitude
598 black carbon and light-scattering aerosols from the boundary layer to the lower stratosphere, *J. Geophys. Res.*, 111, D16207,
599 10.1029/2006jd007076, 2006.

600 Schwarz, J. P., Doherty, S. J., Li, F., Ruggiero, S. T., Tanner, C. E., Perring, A. E., Gao, R. S., and Fahey, D. W.: Assessing
601 Single Particle Soot Photometer and Integrating Sphere/Integrating Sandwich Spectrophotometer measurement techniques
602 for quantifying black carbon concentration in snow, *Atmos. Meas. Tech.*, 5, 2581–2592, 10.5194/amt-5-2581-2012, 2012.

603 Schwarz, J. P., Perring, A. E., Markovic, M. Z., Gao, R. S., Ohata, S., Langridge, J., Law, D., McLaughlin, R., and Fahey, D.
604 W.: Technique and theoretical approach for quantifying the hygroscopicity of black-carbon-containing aerosol using a single
605 particle soot photometer, *J. Aerosol Sci.*, 81, 110–126, <http://dx.doi.org/10.1016/j.jaerosci.2014.11.009>, 2015.

606 Sigl, M., Abram, N. J., Gabrieli, J., Jenk, T. M., Osmont, D., and Schwikowski, M.: 19th century glacier retreat in the Alps
607 preceded the emergence of industrial black carbon deposition on high-alpine glaciers, *The Cryosphere*, 12, 3311–3331,
608 10.5194/tc-12-3311-2018, 2018.

609 Stephens, M., Turner, N., and Sandberg, J.: Particle identification by laser-induced incandescence in a solid-state laser cavity,
610 *Appl. Opt.*, 42, 3726–3736, 10.1364/AO.42.003726, 2003.

611 Wang, M., Xu, B., Kaspari, S. D., Gleixner, G., Schwab, V. F., Zhao, H., Wang, H., and Yao, P.: Century-long record of black
612 carbon in an ice core from the Eastern Pamirs: Estimated contributions from biomass burning, *Atmos. Environ.*, 115, 79–
613 88, <https://doi.org/10.1016/j.atmosenv.2015.05.034>, 2015.

614 Wendl, I. A., Menking, J. A., Färber, R., Gysel, M., Kaspari, S. D., Laborde, M. J. G., and Schwikowski, M.: Optimized
615 method for black carbon analysis in ice and snow using the Single Particle Soot Photometer, *Atmos. Meas. Tech.*, 7, 2667–
616 2681, 10.5194/amt-7-2667-2014, 2014.

617 Zdanowicz, C. M., Proemse, B. C., Edwards, R., Feiteng, W., Hogan, C. M., Kinnard, C., and Fisher, D.: Historical black
618 carbon deposition in the Canadian High Arctic: a >250-year long ice-core record from Devon Island, *Atmos. Chem. Phys.*,
619 18, 12345–12361, 10.5194/acp-18-12345-2018, 2018.

620 Zennaro, P., Kehrwald, N., McConnell, J. R., Schüpbach, S., Maselli, O. J., Marlon, J., Vallelonga, P., Leuenberger, D.,
621 Zangrando, R., Spolaor, A., Borrotti, M., Barbaro, E., Gambaro, A., and Barbante, C.: Fire in ice: two millennia of boreal
622 forest fire history from the Greenland NEEM ice core, *Clim. Past*, 10, 1905–1924, 10.5194/cp-10-1905-2014, 2014.

623

624